

Chandra Observation of the Anomalous X-ray Pulsar 1E 1841-045

Mikio MORII¹, Rie SATO¹, Jun KATAOKA¹, and Nobuyuki KAWAI^{1,2}

¹*Tokyo Institute of Technology, 2-12-1, Ohokayama, Meguro-ku, Tokyo 152-8551*
morii@hp.phys.titech.ac.jp

²*The Institute of Physical and Chemical Research, 2-1, Hirosawa, Wako-shi, Saitama 351-0198*

(Received 2002 December 17; accepted 2003 March 24)

Abstract

We present the results from the *Chandra* ACIS CC mode observation of an anomalous X-ray pulsar (AXP) 1E 1841-045. This is the first observation in which the pulsar spectrum in wide energy range is spatially discriminated from the surrounding SNR, Kes 73. Like other AXPs, the phase-integrated spectrum is fitted well with power-law plus blackbody model. The spectral parameters are $\Gamma = 2.0 \pm 0.3$, $kT_{\text{BB}} = 0.44 \pm 0.02$ keV, and $N_H = 2.54^{+0.15}_{-0.13} \times 10^{22} \text{cm}^{-2}$. This photon index is significantly flatter than the other AXPs, and resemble to soft gamma-ray repeaters (SGRs) in the quiescent state. The pulse profile is double-peaked, and we found that the second peak has significantly hard spectrum. The spectra of all phases are consistent with power-law plus blackbody model with constant temperature and photon index. When fitted with two blackbody model, we obtained similarly good fit. These results can be interpreted that there are two emission regions with different energy spectra.

Key words: stars: pulsars: individual (1E 1841-045) — X-rays: individual (1E 1841-045) — ISM: supernova remnants — ISM: individual (Kes 73)

1. Introduction

The anomalous X-ray pulsars (AXPs) make a small, but unique group (5 or 6) in the X-ray pulsars (~ 100). Their characteristics are as follows (see Mereghetti *et al.* 2002 for a review); (1) much softer X-ray spectra than the more common high mass X-ray binary pulsars, (2) the steady spin-down on the timescales of $10^3 - 10^5$ yrs, (3) spin periods narrowly range in $\sim 5 - 12$ s. AXPs are mysterious, since their energy source is still unknown. First of all, they cannot be rotation-powered, because observed X-ray luminosities ($L_X \sim 10^{34} - 10^{36}$ ergs/s) exceed the spin-down energy loss rates of the neutron stars ($\dot{E} = 4\pi^2 I \dot{P} / P^3 \sim 10^{32.5}$ ergs/s). Secondly, they are unlikely accretion-powered, because any binary companion stars, which provide the accreting mass to the neutron stars, have not been detected.

The most plausible and exotic hypothesis is that AXPs are isolated neutron stars with ultra-strong magnetic field ($\sim 10^{14} - 10^{15}$ G), so-called “Magnetar” (Thompson & Duncan 1993). In this model the X-ray photons are produced by the release of strong magnetic energy stored in the neutron star crust (Thompson & Duncan 1996). Due to the strong magnetic field ($B \gtrsim B_{\text{cr}} = m_e^2 c^3 / e \hbar = 4.4 \times 10^{13}$ G), exotic QED processes are predicted: photon splitting and vacuum polarization, etc.

There are another type of magnetar candidate: soft gamma-ray repeaters (SGRs). AXPs and SGRs exist on a similar region in $P-\dot{P}$ diagram. The persistent X-ray luminosities of SGRs are also much larger than their spin-down luminosities. In contrast to AXPs, SGRs show occasional short bursts, and have relatively harder spectra

($\Gamma \sim 2$) and stronger magnetic fields than those of AXPs (Marsden & White 2001).

1E 1841-045 was discovered as a compact X-ray source centered in a supernova remnant (SNR) Kes 73 (G27.4+0.0) by *Einstein* HRI (Kriss, *et al.* 1985). The kinematic distance toward the SNR was determined to be between 6 and 7.5 kpc, by using the H I absorption data obtained with the VLA (Sanbonmatsu & Helfand 1992). The X-ray pulsation of 11.8 s period was discovered with *ASCA* (Vasisht & Gotthelf 1997) and the central source has been identified as an anomalous X-ray pulsar. Although 1E 1841-045 was observed with *Ginga*, *ROSAT*, *ASCA*, *RXTE* and *BeppoSAX* (Helfand *et al.* 1994, Gotthelf & Vasisht 1997, Gotthelf *et al.* 1999; 2002), pulsar component could not be studied separately from the surrounding SNR component. In this paper we report the spatially resolved spectroscopy of 1E 1841-045 for the first time with *Chandra* thanks to its high spatial resolution of $\sim 0.5''$ (FWHM).

2. Observation and data reduction

Kes 73 and 1E 1841-045 at its center were observed with *Chandra* using the Advanced CCD Imaging Spectrometer (ACIS) in timed exposure (TE) mode (30ks) on 2000 July 23 and continuous clocking (CC) mode (10ks) on 2000 July 29. The image of Kes 73 taken in the TE mode is shown in Figure 1. The source was placed on the nominal target position of ACIS-S3, a back-illuminated CCD on the spectroscopic array (ACIS-S) with good charge transfer efficiency and spectral resolution (Townsend, *et al.* 2002). In addition to S3, four front-illuminated CCDs were active (I0, I1, I2, I3, and S2). The focal plane oper-

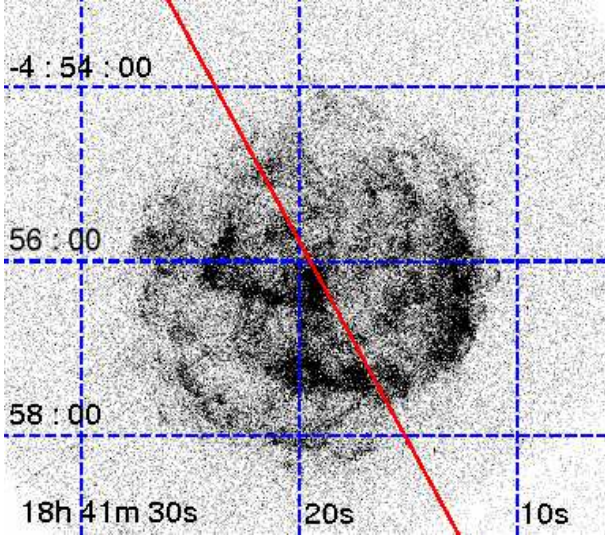


Fig. 1. The image of Kes 73 on the ACIS-S3 chip in TE mode. Coordinates are J2000. The projection axis in CC mode is shown in the slanted line.

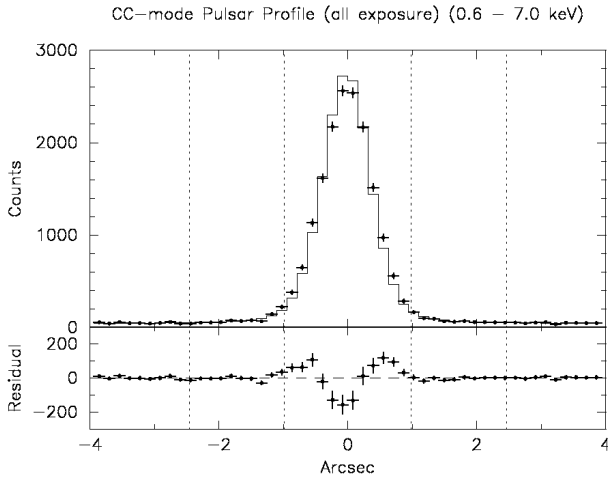


Fig. 2. One-dimensional image of 1E 1841-045 obtained in CC mode (the upper panel). Horizontal and vertical axes are shown in units of arcsec and total counts during all exposure, respectively. Data and their 1σ errors are shown in crosses. The boundaries of the source and background regions are shown by vertical dotted lines (see text). The best fit model consisting of a point source and a constant background is shown by a solid histogram. The residual from the best-fit model is shown in the bottom panel.

ating temperature was -120°C .

For the pulsar analysis, we have used the CC mode data of level 2 product made by the *Chandra* X-ray Center. The net exposure was 10.497 ks. In CC mode, the pileup effect is negligibly small because readout is very short (2.85 ms). It enables us both accurate time-integrated and pulse-phase resolved spectroscopy of the pulsar, but the image is degenerated into one-dimensional.

The projected image around the pulsar in the energy range of 0.6–7.0 keV is shown in Figure 2. We selected

the source photons from the 4 pixels width ($\sim 2''$) centered on the peak pixel. The background has been taken from two segments adjacent to the source region. They are net 6 pixels ($\sim 3''$) wide in total, thus 1.5 times larger than the source region. The background flux amounts to 5.9% of the source flux in the 0.6–7.0 keV energy range.

3. Timing Analysis

The event arrival times have been corrected to the value at the solar system barycenter using *axbary* (CIAO v2.2.1), which utilizes the JPL planetary ephemeris DE-405. We have investigated the light curves of the pulsar with binnings of 0.1, 1.0, 4.0, 16.0, and 64.0 s. We could not find any significant variations of the count rate. We calculated the pulse period by means of the epoch folding method using *efsearch* v1.1 (XRONOS v5.19). The resultant pulse period at reference epoch MJD 51,754 is 11.776(1) s (1σ error). This period is consistent with the spin-down history of the pulsar (Gotthelf, *et al.* 2002). The background-subtracted pulse profile of 0.6–7.0 keV band is shown in Figure 3 (the top panel), where two peaks can be seen clearly as seen with *RXTE* (Gotthelf, *et al.* 2002).

The background-subtracted pulse profiles in the soft energy band (0.6–3.0 keV) and hard energy band (3.0–7.0 keV) are also shown in Figure 3. The second peak around phase 0.8 is larger in the harder energy band. This feature can be seen as an excess of the hardness ratio (Fig 3 fourth panel). This excess is statistically significant at 99.3% confidence level (C.L.).

The background-subtracted peak-to-peak pulse fraction $((F_{\text{max}} - F_{\text{min}})/(F_{\text{max}} + F_{\text{min}}))$ in the 0.6–7.0 keV band, as defined in Özel *et al.* (2001), is $18.9 \pm 2.6\%$ (1σ error).

4. Spectral Analysis

The source and background spectra and response files have been generated using the CIAO v2.2.1 tools *dmextract*, *mkrmf*, and *mkarf*. The extraction has been performed in pulse-invariant (PI) space. The spectrum have been grouped into bins, each of those contains at least 50 events. All the spectral fits have been limited to the 0.6–7.0 keV band and XSPEC v11.2.0 have been used.

4.1. Phase-integrated Spectroscopy

We have fitted the spectrum with a power-law function, blackbody, and thermal-bremsstrahlung models with photoelectric absorption N_H . The blackbody and thermal-bremsstrahlung models are statistically unacceptable at more than 99.9% C.L. The power-law function is also unacceptable at 99.2% C.L. We have also fitted the spectrum with power-law plus blackbody model, and of two blackbodies. Both are acceptable with $\chi^2/dof = 224.6/202$ and $225.8/202$, respectively (see Table 1).

The spectrum and the best-fit power-law plus blackbody model are shown in Figure 4. A dip structure around 1.6 keV is a spurious feature due to the K-edge of aluminum in the optical blocking filter covering the CCD

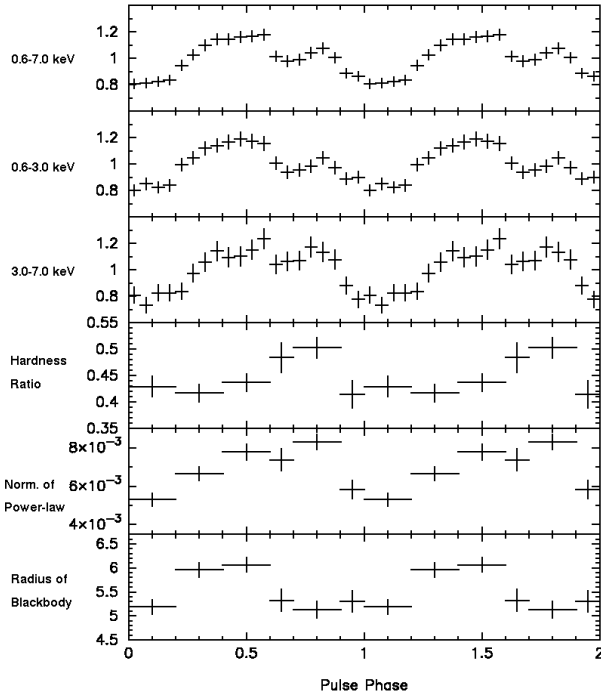


Fig. 3. Folded pulse profiles in the energy ranges of 0.6–7.0 keV, 0.6–3.0 keV, and 3.0–7.0 keV (top three panels). The vertical axes are shown in units of the counts rate normalized to the average counts rate. The fourth panel shows the hardness ratio, the ratio of the photon counts in the hard energy band (3.0–7.0 keV) to the soft energy band (0.6–3.0 keV). The bottom two panels show the normalization of the power-law and the radius (km) of the blackbody emission region on the neutron star surface, assuming the absorbed power-law plus blackbody model with fixed N_H to the best-fit (Table 1), and the source distance is 7 kpc. The horizontal axes are shown in units of pulse phase up to 2 periods. The vertical errors in all panels are 1σ level. In all cases, the backgrounds are subtracted in the way described in § 2.

(*Chandra* Help Desk; private communication).

When fitted with power-law plus blackbody model, the unabsorbed flux in the energy range of 0.6–7.0 keV is 5.0×10^{-11} ergs s $^{-1}$ cm $^{-2}$, and the blackbody component contributes to 48% of the total unabsorbed flux. Assuming a source distance of $d = 7.0d_7$ kpc, X-ray luminosity in the energy range of 0.6–7.0 keV is $2.9 \times 10^{35}d_7^2$ ergs s $^{-1}$, and the radius of blackbody emission region is $R_{BB} = 5.5^{+0.6}_{-0.4}d_7$ km.

When fitted with two blackbodies, the unabsorbed flux in the energy range of 0.6–7.0 keV is 4.1×10^{-11} ergs s $^{-1}$ cm $^{-2}$, and the low temperature blackbody component amounts to 75% of the total unabsorbed flux. Assuming a source distance of $d = 7.0d_7$ kpc, X-ray luminosity in the energy range of 0.6–7.0 keV is $2.4 \times 10^{35}d_7^2$ ergs s $^{-1}$, and the radii of the blackbody emission regions with the low and high temperatures are $R_{low} = 5.7^{+0.6}_{-0.5}d_7$ km and $R_{high} = 0.36^{+0.08}_{-0.07}d_7$ km, respectively.

To compare the flux with the past observations, we calculate the absorbed and unabsorbed flux in the energy range of 1.0–10.0 keV, assuming the best-fit absorbed power-law function spectrum. The results are 1.9×10^{-11}

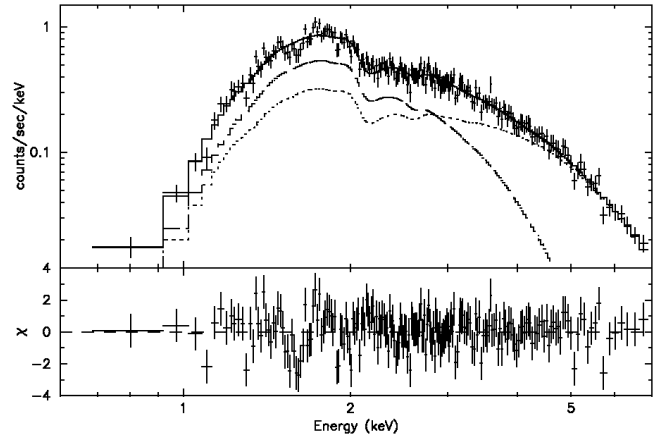


Fig. 4. The upper panel: the background-subtracted pulsar spectrum (cross) and the absorbed power-law plus blackbody model spectrum with the best fitting parameters in Table 1 (solid histogram). The power-law and blackbody components of this model are shown in the dotted and dashed histograms, respectively. The bottom panel: the residual of the source counts from the best-fit model.

ergs s $^{-1}$ cm $^{-2}$ and 6.8×10^{-11} ergs s $^{-1}$ cm $^{-2}$, respectively. Those values are consistent with *ASCA* observations (Vasisht & Gotthelf 1997, Gotthelf & Vasisht 1997, and Mereghetti *et al.* 2002).

4.2. Phase-resolved Spectroscopy

To search for possible spectral variations as a function of the pulse phase, we have divided the data into six phase intervals: off-pulse (0.0–0.2), rising (0.2–0.4), top of the first pulse (0.4–0.6), valley (0.6–0.7), top of the second pulse (0.7–0.9), and off-pulse (0.9–1.0) (see Figure 3). We have fitted all phases with absorbed power-law function plus blackbody model, where the column density N_H at each phase is fixed to the best value obtained in §§ 4.1. Due to the limited photon statistics, the fitting with no constraint is not possible. Therefore, we first fixed only the power-law index, or blackbody temperature. In either case, fits for all phases are acceptable within 90% C.L., and the blackbody temperatures or the power-law indices show no significant deviations from the mean values. Then, we fixed the blackbody temperature and photon index to the best-fit values obtained in §§ 4.1 and normalizations are allowed to vary. In this case all fits are also acceptable within 90% C.L. The variation of the normalizations are shown in Figure 3. The normalization of the blackbody varies in sinusoidal form, while that of the power-law component does not. In Figure 3, the blackbody normalizations are shown as the radii of the emission region on the neutron star surface, assuming a distance of 7.0 kpc.

We have repeated the similar procedure for the absorbed two blackbody model. We obtained essentially the same result with the previous model, where the normalization of the power-law component is replaced with the higher temperature blackbody component in the bottom panels of Figure 3.

Table 1. Phase-Integrated spectrum fitting parameters with 1σ errors. Notation of the models are as follows; PL: Power-law, BB: Blackbody, TB: thermal-bremsstrahlung.

Model	Γ	$kT(\text{keV})$	R_{BB} (km)	N_H (10^{22}cm^{-2})	χ^2/dof
PL	3.28 ± 0.05	—	—	3.25 ± 0.06	$255.7/204 = 1.25$
BB	—	0.69	2.4	1.6	$617.7/204 = 3.03$
TB	—	2.01 ± 0.06	—	2.52 ± 0.04	$330.0/204 = 1.62$
PL + BB	2.0 ± 0.3	0.44 ± 0.02	$5.5^{+0.6}_{-0.4}$	$2.54^{+0.15}_{-0.13}$	$224.6/202 = 1.11$
BB + BB	—	$0.47 \pm 0.02/1.5^{+0.2}_{-0.1}$	$5.7^{+0.6}_{-0.5}/0.36^{+0.08}_{-0.07}$	2.34 ± 0.08	$225.8/202 = 1.12$

5. Spatial search for extended nebula

We fit the one-dimensional CC mode image with a model consisting of a point source (pulsar) and a constant background (SNR), and evaluated the normalizations of the two components. To simulate the point source, we used *MARX* v4.0 and input the best-fit power-law plus blackbody model spectrum, obtained in §§ 4.1. The model with the best-fit normalizations is shown in Figure 2. The residual from the model is largest at ± 0.5 arcsec, indicating that the image is more extended than the point spread function by ~ 0.5 arcsec (≈ 1 pixel). We, however, do not consider this spatial extent to be significant, because the image is constructed with dithering and rotation, and is unavoidably blurred to an order of 1 pixel.

We then estimated the upper limits for a possible pulsar nebula flux. We fit the image with a model including a point source, extended nebula, and constant background. The nebula is simulated by *MARX* v4.0 as a sphere filled with uniform emissivity centered on the point source, and the spectrum is the absorbed power-law model with a photon index of $\Gamma = 2.0$ and $N_H = 2.54 \times 10^{22}\text{cm}^{-2}$. We obtained upper limits for the nebula with radii of 1.0 and 3.0 arcsec to be 3.0×10^{-12} ergs $\text{s}^{-1} \text{cm}^{-2}$ and 3.7×10^{-13} ergs $\text{s}^{-1} \text{cm}^{-2}$ in the energy range of 0.6–7.0 keV, respectively.

6. Discussion

Thanks to the unprecedented spatial resolution of *Chandra*, the pulsar spectrum is clearly discriminated from the surrounding SNR for the first time. Before this observation, this source is only fitted with a power-law function, then resulting in the power-law index of $\Gamma = 3.4 \pm 0.3$ by *ASCA* (0.9–8.0 keV) (Gotthelf & Vasisht 1997) and $\Gamma \simeq 2.0$ by *RXTE* (2–10 keV) (Gotthelf, *et al.* 2002).

In our analysis, we find that the power-law plus blackbody model is preferred to a single power-law function, where the best spectral parameters are $\Gamma = 2.0 \pm 0.3$, $kT_{BB} = 0.44 \pm 0.02$ keV, and $N_H = 2.54^{+0.15}_{-0.13} \times 10^{22}\text{cm}^{-2}$. This spectral model may be typical for AXPs, because four AXPs, 1E 2259+586, 4U 0142+61, 1E 1048.1-5937, and 1RXS J170849.0-400910 are also fitted with this model (e.g. Mereghetti *et al.* 2002). The blackbody temperature of 1E 1841-045 is similar to these four AXPs, but the power-law index is significantly flatter than that of others ($\gtrsim 3$). This value is close to that of SGRs (~ 2), and its estimated dipole magnetic field ($B = 3.3 \times 10^{19}(\text{P}\dot{\text{P}})^{1/2} = 7.3 \times 10^{14}$ G) is also close to that of SGRs

(Marsden & White 2001); 5.9×10^{14} G for SGR 1900+14 and 9.7×10^{14} G for SGR 1806-20. From these aspects, 1E 1841-045 is the closest object to SGRs among AXPs.

The radius of the blackbody emission region is $5.5^{+0.6}_{-0.4} d_7$ km. This is smaller than the whole neutron star surface, but yet much greater than the polar cap hot spot expected for magnetically channeled accretion. Furthermore, the blackbody radius varies with pulse phases in sinusoidal form, suggesting the inhomogeneous distribution of the temperature on the neutron star surface, which might be caused by non-isotropic heat conduction (Greenstein & Hartke 1983), or heating due to magnetic field decay.

Spectral hardening at the second peak is found for the first time. This feature could be attributed to an excess of the power-law component at that phase, when fitted with a power-law plus blackbody model. Since the phase of maximal normalization of the power-law component is different from the blackbody maximum, the emission region of the power-law component is clearly displaced from the hot thermal region. We also obtained a good fit for a two-blackbody model. Therefore, we can interpret those that there are two emission regions with different energy spectra; one is a hot spot on the neutron star surface which emits lower temperature blackbody radiation, and the other is a non-thermal source presumably in the magnetosphere, or another hot spot on the neutron star surface with a higher temperature.

References

- Gotthelf, E. V. & Vasisht, G. 1997, ApJ, 486, L133
- Gotthelf, E. V. et al. 1999, ApJ, 522, L49
- Gotthelf, E. V., et al. 2002, ApJ, 564, L31
- Greenstein, G. & Hartke, G. J. 1983, ApJ, 271, 283
- Helfand, D. J. et al. 1994, ApJ, 434, 627
- Kriss, G. A., et al. 1985, ApJ, 288, 703
- Marsden, D & White, N. E. 2001, ApJ, 551, L155
- Mereghetti, S. et al. 2002, astro-ph/0205122
- Özel, F. et al. 2001, ApJ, 563, 255
- Sanbonmatsu, K. Y & Helfand, D. J. 1992, Astron. J., 104, 2189
- Thompson, C. & Duncan, R. C. 1993, ApJ, 408, 194
- Thompson, C. & Duncan, R. C. 1996, ApJ, 473, 322
- Townsley, L. K. et al. 2002, Nucl. Instr. and Meth. A, 486, 751
- Vasisht, G. & Gotthelf, E. V. 1997, ApJ, 486, L129